Fluctuating hydrodynamics simulations of coarse-grained lipid membranes under steady-state conditions and in shear flow

Erik G. Brandt

Fluctuating Hydrodynamics Simulations of Coarse-Grained Lipid Membranes Under Steady-State Conditions and in Shear Flow

Erik G. Brandt*

Department of Materials and Environmental Chemistry, University of Stockholm, Sweden

Abstract

The stochastic Eulerian-Lagrangian method (SELM) is used to simulate coarse-grained lipid membrane models under steady-state conditions and in shear flow. SELM is an immersed boundary method which combines the efficiency of particle-based simulations with the realistic solvent dynamics provided by fluctuating hydrodynamics. Membrane simulations in SELM are shown to give structural properties in accordance with equilibrium statistical mechanics and dynamic properties in agreement with previous simulations of highly-detailed membrane models in explicit solvent. Simulations of sheared membranes are used to calculate surface shear viscosities and inter-monolayer friction coefficients. The membrane models are shown to be shear-thinning under a wide range of applied shear rates.

_____

* e-mail: erik.brandt@mmk.su.se

FIG. 1. (Color online) Schematic view of the hydrodynamic interaction (HI): Two particles (depicted as red spheres) immersed in a fluid are forced to adjust to the local velocity field (small solid arrows) which is mediated by the fluid over long distances. The net forces (large dashed arrows) tend to move the particles in the flow direction. Contributions from thermal fluctuations makes the nanoscale velocity field irregular, as described by the equations of fluctuating hydrodynamics.
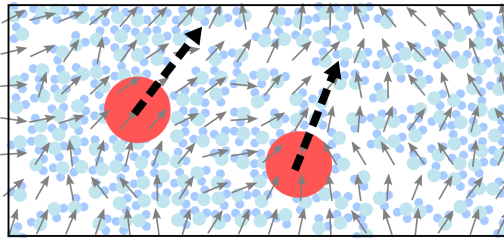
I. INTRODUCTION

Many components in soft matter can be described as elastic microstructures immersed in ambient fluid (typically water). These structures include lipids, proteins, and nucleic acids, and their interactions with the surrounding fluid are fundamental to molecular biology [1]. Their ability to form hydrogen bonds with water molecules is the microscopic origin of the hydrophobic interaction that drives protein folding and aggregation of lipids and surfactants [2]. Hydrodynamic interactions (HI) are mediated by the embedding fluid (Fig. 1) as the counterforce exerted between these microstructures when they are forced to adopt to the local fluid velocity [3]. Lipid molecules aggregate in water, and form a variety of ordered membrane structures under physiological conditions [4]. Lipid membranes resemble two-dimensional fluids, but are free to adjust global shape by deforming into the normal direction, and local shape by molecular reorientation [5]. Hydrodynamic interactions play a key role in membrane dynamics not only for undulations [6], but for membrane-bound protein diffusion [7] and membrane domain formation [8].

HI are dictated by the fluid velocity, which is given by the Navier-Stokes (NS) equations for the flow geometry at hand. On the nanometer length scales relevant to soft matter hydrodynamics, the velocity field is highly irregular because of thermal fluctuations [9]. These are not described by the NS equations, but were first treated in the extended theory of Landau and Lifshitz [10]. The modified Navier-Stokes equations of Landau and Lifshitz have been referred to as the equations of fluctuating hydrodynamics (FH), and have been

shown to be valid at the molecular scale [11]. In general, numerical simulations are required to determine hydrodynamic interactions. Molecular dynamics (MD) simulations are used to integrate the equations of motion of both immersed particles and solvent particles. MD has been used to study fluctuations in lipid membranes [12, 13], although length- and time scales are restricted to $\sim$10 nm and $\sim$100 ns. Coarse-graining (CG) by lumping molecular groups into beads with effective interactions broadens this window. The solvent can be completely ignored in equilibrium studies and its cohesive effect included implicitly. This has been used with remarkable success in equilibrium studies of lipid membranes [14–16], but obviously fails when HI are prevalent. The implicit solvent approach is attractive for membrane simulations because the solvent particles outnumber the lipid molecules by more than 10:1. The friction effect of the solvent is taken into consideration by integrating a set of coupled Langevin equations for the positions of the immersed particles [17]. First-order hydrodynamic effects can further be included with the use of the well-known solution to Stokes flow (often referred to as Stokesian-Brownian dynamics [18, 19]). Direct numerical simulation (DNS) of the Navier-Stokes equations is a more accurate treatment of the solvent, where the dynamics of the immersed particles enter as boundary conditions on the fluid motion. It is costly in terms of computer time to resolve the boundaries between the particles and the fluid. Peskin [20, 21] therefore proposed the immersed boundary (IB) method: a reformulation of the hydrodynamic equations in which the fluid and the structures overlap. The immersed particles are conceptual fluid "blobs" where additional forces act. These forces are local and therefore cheap to calculate.

The equations of fluctuating hydrodynamics can be cast in the form of an IB method [22, 23] to include thermal motions of soft matter. The aim of the present work is to apply such a stochastic immersed boundary method to coarse-grained lipid membrane models. Membrane models originally designed for implicit solvent can be utilized with this method to obtain realistic dynamic properties of lipid membranes [24]. The simulation method covers shear flow [25], and surface shear viscosities and inter-monolayer friction coefficients are calculated for the membrane models. Overdamped equations of motion from a small-scale approximation are used for the dynamics of the fluid-structure system. This is similar to Stokesian-Brownian dynamics in that only the dynamics of the particles is tracked while hydrodynamic interactions are kept. The simulation method is based on a general formulation of pairwise interacting elementary particles in an incompressible fluid.

II. SELM: STOCHASTIC EULERIAN-LAGRANGIAN METHOD

The Stochastic Eulerian-Lagrangian Method (SELM) [22] describes how fluctuating hydrodynamics (FH) can be adapted to the Immersed Boundary (IB) method developed by Peskin [21]. The acronym refers to that Lagrangian coordinates are used for the immersed structures while the fluid is modeled on a Eulerian grid. Thermal fluctuations are incorporated as random forces whose strengths are determined by the fluctuation-dissipation theorem of statistical mechanics. SELM has been shown to give an internally consistent representation of the FH equations with the Immersed Boundary formulation for general flow situations [22]. The full SELM equations are not needed to describe the quasi-steady-state flows of the present work. Incompressible flow is considered with focus on the small-scale spatial regime where advective transport is negligible, and the immersed structures are modeled as point particles. In contrast to the usual creeping-flow limit (Stokes flow), the explicit time-dependence of the fluid velocity is kept due to rapid thermal fluctuations of the immersed structures.

A. The overdamped equations of motion

An additional simplification can be done on the smallest length scales. The hydrodynamic relaxation of the fluid on a length scale L is associated with the timescale $\tau_{\text{fluid}} = \rho L^2/\eta$, where η is the fluid dynamic viscosity and ρ is the fluid density. The time it takes an immersed particle of radius a to diffuse a distance comparable to its own size is $\tau_{\text{diff}} = (a^2/D) = 6\pi\eta a^3/k_B T$, where D is the diffusion coefficient, and the last equality follows from the Stokes-Einstein relation. The dynamic viscosity and mass density for water at room temperature is $\eta = 10^{-3}$ Pa s and $\rho = 10^3$ kg/m^3. When $L = 5$ nm, the time scales for a particle of size $a = 1$ nm are $\tau_{\text{fluid}} = 2.5 \times 10^{-11}$ s and $\tau_{\text{diff}} = 4.5 \times 10^{-9}$ s, respectively. These separated time scales motivate an approximation in which the fluid velocity instantly adopts to the immersed particles (corresponding to the limit $\eta \to \infty$). This is referred to as overdamped dynamics, since the fluid motion is slaved by the immersed particles.

Only the particle dynamics needs to be tracked, and the full stochastic equations of motion are reduced to [22]

$$\frac{\partial \mathbf{X}_j}{\partial t} = \sum_i \mathcal{M}_{ji}\mathbf{F}_i + \mathbf{g}_j\,, \tag{1}$$

4

for the positions of the immersed particles, $\mathbf{X}_j$. The force on particle j from all the other particles is $\mathbf{F}_j = \sum_i \mathbf{F}_{ji} = -\sum_i \nabla_{\mathbf{X}_j} U(|\mathbf{X}_j - \mathbf{X}_i|)$, with $U(X)$ being a pair potential. Periodic boundary conditions are employed in all directions. $\mathbf{g}_j$ is a random force with zero mean and variance

$$\left\langle \mathbf{g}_j(t)\, \mathbf{g}_i^{\mathrm{T}}(t') \right\rangle = 2 k_B T \mathcal{M}_{ji}(t) \delta(t - t') \,, \tag{2}$$

which is local in time and obeys the fluctuation-dissipation theorem. $\mathcal{M}_{ji}$ is a symmetric matrix operator that conveys the hydrodynamic interaction [26],

$$\mathcal{M}_{ji}(t) = \iint_\Omega \mathrm{d}\mathbf{x}\, \mathrm{d}\mathbf{x}'\, \delta_\Delta \left(\mathbf{x} - \mathbf{X}_j(t) \right) \delta_\Delta \left(\mathbf{x}' - \mathbf{X}_i(t) \right)$$
$$\times \mathcal{O} \left(\mathbf{x} - \mathbf{x}' \right) \,, \tag{3}$$

with $\mathcal{O}\left(\mathbf{r}\right)$ being the Oseen tensor [3],

$$\mathcal{O}(\mathbf{r}) = \frac{\rho}{8\pi\eta\,|\mathbf{r}|} \left(\mathcal{I} + \frac{\mathbf{r}\mathbf{r}^{\mathrm{T}}}{|\mathbf{r}|^2} \right) \,, \tag{4}$$

and where $\mathcal{I}$ is the unit tensor. $\delta_\Delta(\mathbf{x})$ is a smoothed Dirac delta kernel with good numerical properties [21] (details are given in Ref. [27]), which averages the local irregular velocity over a neighborhood determined by the length a (Fig. 2). The integral in Eq. (3) spans the entire domain occupied by the fluid (including the regions overlapping with the immersed particles). Eq. (1) resembles the equations of motion used in Stokesian-Brownian (SB) dynamics [18, 19], but the hydrodynamic operator $\mathcal{M}_{ji}$ is different from the tensors employed in SB dynamics, even in the continuum limit. The difference lies in the hydrodynamic interactions in SELM being averaged over a local neighborhood around the immersed structure (determined by the kernel function length a). The Oseen tensor is the leading-order term in an asymptotic expansion of the hydrodynamic field and becomes inaccurate for small particle separations [28]. More sophisticated hydrodynamic interactions, such as the Rotne-Pragner-Yamakawa (RPY) tensor [29] have been employed in SB simulations [30–32] and can also be incorporated into SELM. However, Eq. (3) reproduces the correct hydrodynamic tensors down to separations of two particle radii [22] which is sufficient for the present work.

B. SELM simulations of shear flow

Shear flow is commonly implemented in molecular simulations with Lees-Edwards boundary conditions [33]. The periodic unit cell is modified by shifting the periodic boxes parallel

FIG. 2. (Color online) Left: Snapshot from coarse-grained lipid membrane simulation employing fluctuating hydrodynamics. The lipid bilayer is modeled by interacting elementary particles (green and gray spheres) on a meshed fluid (green points) with periodic boundaries. Right: Hydrodynamic interactions are handled by averaging the velocity of the immersed structure over the local neighborhood of the fluid field (top). The elementary particle size can be tuned according to application, but is fixed to $a = 4\Delta$ in the present work, with Δ being the mesh size. The particle shape is determined by a kernel function, $\delta_\Delta(r)$ (bottom). All details of the lipid models and the numerical algorithm are given in Ref. [27].
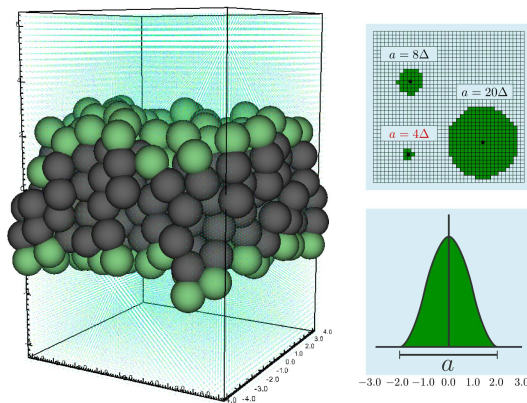
to the shear direction; the result is similar to a wall of sliding bricks [34]. Particles crossing the sliding boundary are reintroduced at positions shifted by $\pm sL_z t$ with respect to the usual periodic positions, where s is the shear rate (units $1/t^0$) and L_z is the box height. The jump in velocity of the shifted particle is $\Delta v = sL_z$, and the minimum image-convention is modified accordingly [35] (since the sliding boundary is not periodic). The Lees-Edwards approach works well to maintain a steady shear flow in particle-based molecular dynamics simulations, but is problematic for mesh-based methods because mesh points do not align at the sliding boundary. This can be circumvented by introducing deformed coordinates in which the mesh is periodic [25]. This has been done for non-Hamiltonian MD simulations [35], Navier-Stokes solvers [36], and recently for fluid-structure interactions in dispersions [37].

The deformed space- and time coordinates $\mathbf{x}' = (x', y', z', t') = (\mathbf{q}', t')$ are related to the Cartesian coordinates $\mathbf{x} = (x, y, z, t)$ by the mapping $\mathbf{x} = \phi(\mathbf{x}') = (x' - st'z', y', z', t')$. The mesh enters the overdamped dynamics when calculating the hydrodynamic operator and indirectly when generating the stochastic driving fields. Substituting in Eq. (3), the

hydrodynamic operator on the periodic $\mathbf{q}$-mesh is

$$
\begin{aligned}
\mathcal{M}_{ji}(t) = \iint_{\Omega} \mathrm{d}\mathbf{q}_1 \, \mathrm{d}\mathbf{q}_2 \, \delta_\Delta \left(\boldsymbol{\phi}(\mathbf{q}_1, t) - \mathbf{X}_j(t) \right) \\
\times \, \delta_\Delta \left(\boldsymbol{\phi}(\mathbf{q}_2, t) - \mathbf{X}_i(t) \right) \mathcal{O}(\boldsymbol{\phi}(\mathbf{q}_1, t) - \boldsymbol{\phi}(\mathbf{q}_2, t)) \,.
\end{aligned} \tag{5}
$$

The volume of the box vector matrix $L_{\alpha\beta}$, with α and β taking the values $\{x, y, z\}$, is conserved since $\det(L_{\alpha\beta}(t)) = \det(L_{\alpha\beta}(0))$. The box is increasingly skewed as the simulation proceeds, but is reset by invoking modular invariance associated with the minimum-image convention [38]: Periodic images are equivalent when $st'L_{xx}/L_{zz} = 1$ and when $st'L_{xx}/L_{zz} = 0$. Thus, L_{xz} is reset to 0 when $st'L_{xx}/L_{zz} = 1$.

C.   Numerical implementation

Eq. (1) is solved numerically with the Euler-Maruyama method [39] and updated iteratively. The discretization is

$$
\mathbf{X}_j^{t+1} = \mathbf{X}_j^t + \sum_i \left[\mathcal{M}_{ji}^t \mathbf{F}_i^t \mathrm{d}t + \sqrt{2 k_B T \mathcal{M}_{ji}^t \, \mathrm{d}t} \boldsymbol{\xi}_i^t \right] \,, \tag{6}
$$

in the Ito formulation, where the t index refers to the iteration step and the j, i index to a pair of immersed particles. $\mathrm{d}t$ is the time step, while $\boldsymbol{\xi}_j$ is a normal distributed random number with zero mean and unity variance. The discretized hydrodynamic operator is defined on a deformed mesh with periodic boundary conditions in all directions. $\mathcal{M}_{ji}$ is a double convolution which is efficiently evaluated in Fourier space, and then inverted back to real space. The square root of $\mathcal{M}_{ji}$ is found by Cholesky factorization. More details on the simulation algorithm are given in Ref. [27].

III.   MEMBRANE MODELS AND SIMULATION PARAMETERS

Coarse-grained membrane models, which implicitly account for hydrophobic interactions to get rid of the solvent, are orders-of-magnitudes faster than atomistic models but can not treat hydrodynamic effects. However, implicit-solvent membrane models are commonly constructed from interacting point particles and can be used off-the-shelf within SELM, to reintroduce the solvent degrees of freedom using fluctuating hydrodynamics. The present work

7

have used two of the most widespread coarse-grained membrane models: The Brannigan-Philips-Brown (BPB) model [15] and the Cooke-Kremer-Deserno (CKD) model [16]. Both models are based on beads and springs, where the lipid molecule is a short polymeric chain that consists of different bead types. Cohesive interactions are added to the tail groups to enforce self-assembled bilayer structures. The fluid bilayer phase is not sensitive to the exact shape of the cohesive potential, but it has to be more long-ranged than a standard Lennard-Jones potential. The BPB model uses five beads while the CKD model uses three beads. The interactions parameters used in the present work were essentially the same as in the original works. More details on the membrane models and the parameters involved are given in Ref. [27].

Coarse-grained molecular dynamics (CG-MD) simulations of the implicit-solvent lipid models were run in LAMMPS (5 May 2012) [40]. SELM was implemented as a module in LAMMPS, and was used to run simulations of the membrane models with (overdamped) fluctuating hydrodynamics. Pre-equilibrated bilayer membrane patches of 8×8 molecules (per monolayer, 128 lipids in total) were obtained from CG-MD simulations at constant zero surface tension (1×10^5 steps). These simulations keep the bilayer in a tensionless state by scaling the lateral box lengths while keeping the box height fixed, with the aim to have equal pressures in the lateral and normal directions. The equilibrated patches were used as starting structures for the production SELM and CG-MD simulations. The simulation parameters are summarized in Table I (using reduced units [27]).

The Peskin δ-function [21, 27] was used for the kernel function $\delta_\Delta(r)$. Its extent was fixed with respect to the mesh width as $a = 4\Delta$, which represents the size of an immersed particle. For the 8×8 patch, 40 mesh points were needed in the membrane's lateral directions to accurately resolve the lipid particles. The influence of the box height was investigated using 60, 80, and 100 mesh points in the normal direction. The CG-MD simulations were run with a Langevin thermostat [41] at constant volume and temperature (NVT ensemble), which corresponds to Brownian dynamics (BD) [34] without hydrodynamic interactions. The thermostat damping parameter ω was varied between $(0.1\text{--}10)/t^0$.

Self-assembly simulations were performed with both SELM and CG-MD, in a fixed simulation box with lateral size corresponding to the equilibrium area per molecule, and with box height that was 2.5 times larger. The simulations were started with 128 lipids in random positions and orientations. Shear simulations were performed within the modified

SELM formalism described in Section II B. The applied shear rates were varied between $s = (0.001\text{--}1.0) / t^0$, and the simulations lasted for 1×10^6 steps. Bootstrapping was used on the time series to determine error bars as 95% confidence intervals.

IV.   RESULTS AND DISCUSSION

The SELM simulations were compared to CG-MD simulations to assess the hydrodynamic effects. It is first shown that SELM reproduces the equilibrium structures expected from statistical mechanics. The self-assembly simulations indicate that the pathway to equilibrium is different when hydrodynamic interactions are included, but the equilibrium ensemble is unchanged. This is emphasized by comparing diffusion rates between SELM and CG-MD. Finally, SELM simulations were used to investigate lipid membranes in shear flow.

TABLE I. Simulation parameters for SELM and CG-MD. Common = Both SELM and CG-MD. SELM = Only SELM.

Parameter	Symbol	Unit	BPB	CKD
Common				
Time step	dt	t^0	0.002	0.01
Number of steps	n	1	1×10^6	1×10^6
Temperature	T	T^0	0.9	1.1
Area per molecule	a_0	σ^2	1.0	1.1
SELM				
Mesh size	Δ	σ	0.2	0.2185
Mesh points in x	N_x	1	40	40
Mesh points in y	N_y	1	40	40
Mesh points in z	N_z	1	60/80/100	60/80/100
Water viscosity	η	η^0	18.15	20.90
Water mass density	ρ	ρ^0	1.815	1.829

FIG. 3. (Color online) Lipid number densities as functions of the distance from the bilayer center. (a) BPB model. Five peaks are visible, one for each bead. There is a pronounced dip in the bilayer center. (b) CKD model. The profile is smoother but different beads can still be distinguished. The absence of a center dip suggests that more lipids flip between the monolayers.
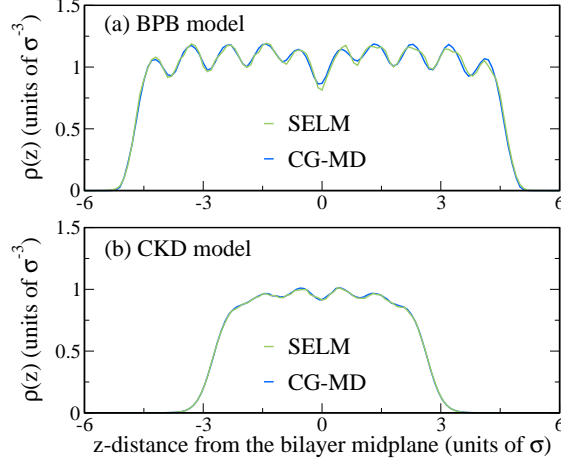

A. Equilibrium properties

The following equilibrium properties were calculated for the membrane models. $\rho(z)$ is the bead density as a function of distance from the bilayer center. $g(r)$ is the in-plane radial distribution function. $S(q)$ is the corresponding in-plane structure factor. Fig. 3 shows $\rho(z)$ for both membrane models, calculated from SELM and CG-MD simulations. Beads show up as distinct peaks in the distribution. There is a dip in the distribution at the bilayer center for the BPB model, showing that the lipid exchange between monolayers is small. This is explained by the strong cohesive interactions that are focused to the single interface bead in the BPB model, and not distributed over the tail beads as in the CKD model. The $\rho(z)$-profiles from the SELM simulations are almost identical to the CG-MD simulations. The location of the peaks are particularly well-matched. Fig. 4 shows the two-dimensional radial distribution function (rdf) of the lipid models, defined by

$$g(r) = \frac{1}{N\rho_0} \left\langle \sum_{i \neq j}^{N} \delta\left(\mathbf{r} - \mathbf{r}_{ij}\right) \right\rangle, \qquad (7)$$

where $\mathbf{r}_{ij}$ is the in-plane separation vector between bead i and j, and $\rho_0 = N/A$ is the bulk number density, with N being the number of lipids per monolayer, and A being the total area. $g(r)$ measures the bilayer's lateral structure without accounting for height correlations. For infinite separations, $g(r \to \infty) = 1$ as expected, the dimensionless equivalence to the

FIG. 4. (Color online) The (in-plane) radial distribution function (rdf) of (a) the BPB model and (b) the CKD model for the CG-MD simulations (blue) and the SELM (green) simulations. The two lines completely overlap. The insets shows the static structure factors for the models, which are isotropic Fourier transform of the rdfs.
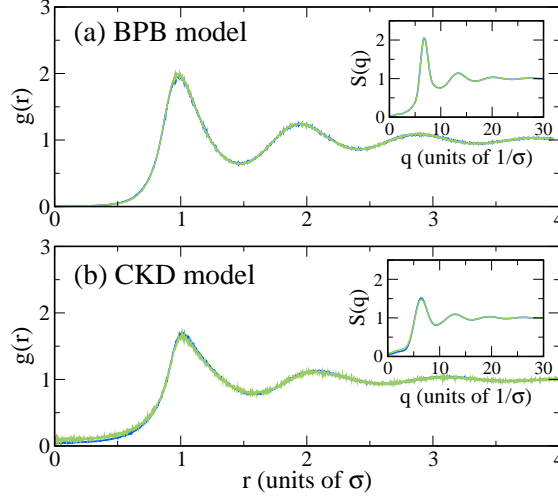
bulk number density (inverse area per lipid) $\rho_0 = a_0^{-1}$. The insets in Fig. 4 show the corresponding structure factors,

$$S(q) = \frac{1}{N} \langle \rho(q) \rho^*(-q) \rangle \, , \tag{8}$$

which are the fluctuation spectra of the Fourier components of the in-plane bead density, $\rho(q) = \frac{1}{N} \sum_{i=1}^{N} e^{-i\mathbf{q} \cdot \mathbf{r}_i}$, where $\mathbf{r}_i$ is the position of bead i. $S(q)$ and $g(r)$ are related by a Fourier transform. The large-q limit of $S(q)$ corresponds to vanishing correlations at small distances, while the small-q limit is given by the compressibility relation [42]

$$\lim_{q \to 0} S(q) = \frac{2k_B T}{a_0 K_A} \, , \tag{9}$$

where K_A is the bilayer area compressibility (twice the monolayer compressibility), and a_0 is the area per molecule. Investigating the $q \to 0$ limits yields $K_A^{\mathrm{BPB}} \approx K_A^{\mathrm{CKD}} \approx 20\,\epsilon/\sigma^2$, which translates to $K_A^{\mathrm{BPB}} \sim 300$ mN/m and $K_A^{\mathrm{CKD}} \sim 200$ mN/m in physical units, in good agreement with known equilibrium values for the models [15, 16] and with experimental data [43]. The equilibrium membrane structures of the SELM and CG-MD simulations are almost identical, demonstrating that SELM samples the appropriate Gibbs-Boltzmann distribution.

FIG. 5. (Color online) Snapshots from self-assembly simulation of the CKD model. The pathway to equilibrium is similar for the SELM (top row) and CG-MD (bottom row) simulations but the time scales differ by a factor 20.
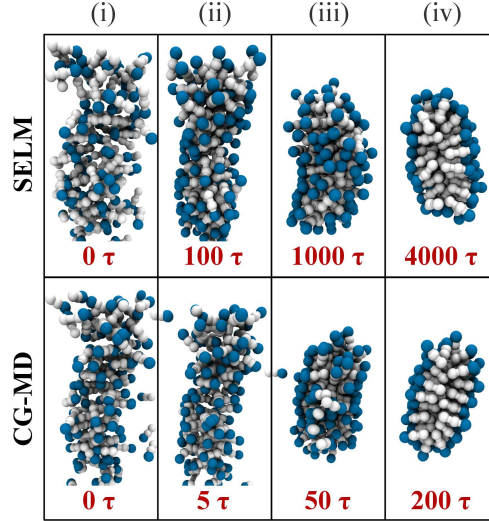
B. Self-assembly

The coarse-grained membrane models used in the present work are generic hydrophilic head/hydrophobic tail-like lipids. The hydrophobic interactions in the BPB model are focused to the interface bead, while the tail attractions are relatively weak. In the CKD model hydrophobicity is distributed by the long-range potential across both tail beads. The simulation parameters and the temperature were chosen to represent fluid membranes at physiological temperatures (Table I). The temperatures were identified to be slightly below room temperature (270 K) for the BPB model (the same temperature was used in Ref. [5]) and room temperature (300 K) for the CKD model. Thermal fluctuations are inhibited and equilibration is expedited at the lower temperature used for the BPB model. The self-assembly simulations were found to result in very similar equilibrium structures (Fig. 5), but the absolute time scale was 20 times slower with SELM than with CG-MD. The bilayer formation followed the same pathway in the SELM and the CG-MD simulations. From the random starting configuration (i), an elongated stalk-like structure formed rapidly (ii). The free energy is then minimized by shielding the hydrophobic tail groups (iii), which compresses the stalk into a spherical cap-like structure. This configuration is metastable and can persist for long times. Eventually, energetically favorable interactions are found with

12

FIG. 6. (Color online) Lateral mean-square-displacement of the lipid center-of-mass (COM) for the BPB [(a) and (c)] and CKD [(b) and (d)] models. The top panels are SELM simulations with different box heights. The bottom panels are coarse-grained MD (CG-MD) simulations with a Langevin thermostat, using different values for the damping parameter ω.
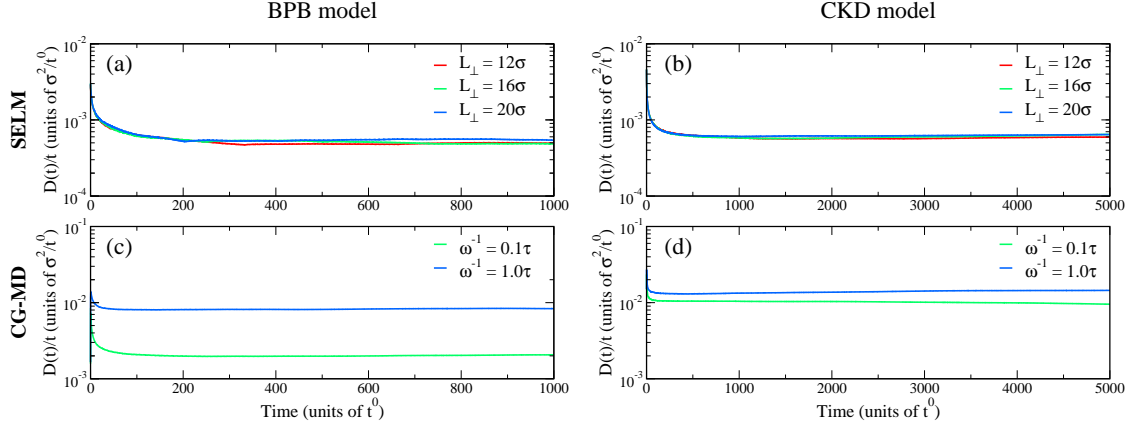
periodic neighbor molecules, leading to the formation of a lamellar phase (iv). If the simulation is allowed to proceed, the lipid molecules align to form a perfect bilayer, although this may take a very long time.

The slower dynamics of the BPB model compared to the CKD model can be attributed to the strong interactions between the interface beads in the BPB model. The BPB lipids form monolayers that diffuse randomly before finding bilayer configurations, which is a slow process. The long-range forces used in both models to mimic the hydrophobic effect are of molecular origin, and are not accounted for by the fluctuating hydrodynamics in SELM, which only transfers momentum by viscous diffusion.

C. Lateral diffusion

The lateral mean-square-displacement (MSD) is

$$D(t) = \frac{1}{4} \left\langle (\mathbf{r}_i(t) - \mathbf{r}_i(0))^2 \right\rangle . \tag{10}$$

The factor 4 is specific to a two-dimensional system (in general this factor is $2d$, where d is the system dimensionality) and $\mathbf{r}_i = (x_i, y_i)$ is the in-plane coordinate of lipid i. Eq. (10) applies to atomic coordinates as well as to molecular center-of-mass (COM) coordinates. The brackets denote an ensemble average over all positions and starting times. The self-diffusion

13

coefficient is determined from the long-time limit of Eq. (10) according to

$$D_{\text{lat}} = \lim_{t \to \infty} \frac{\mathrm{d}D(t)}{\mathrm{d}t} \,. \tag{11}$$

D_{lat} is constant if $D(t)$ is linear in time in the limit $t \to \infty$ ($D(t)/t$ tends to a constant). Fig. 6 shows semi-logarithmic plots of $D(t)/t$ for the COM of the membrane models, from SELM and CG-MD simulations, where D_{lat} is obtained as the asymptotic value of $D(t)/t$. The initial slope of $D(t)$ is strongly non-linear, but gradually decreases. $D(t)/t$ reach asymptotic values after $200\,t^0$. Varying the box height in the SELM simulations changed D_{lat} by $\sim 10\%$ but did not modify the general trend of the MSD (data not shown). D_{lat} from the SELM simulations are similar for both membrane models, $(5\text{--}10) \times 10^{-4}\,\sigma^2/t^0$. This corresponds to roughly 50–100 $\mu\text{m}^2/\text{s}$ in physical units [27], which is similar to experimental values (see Ref. [44] and the references therein), depending slightly on the measurement technique.

It is encouraging that the diffusion rates obtained for the two models from the SELM simulations are in such good agreement. Given the similarity of the models in spirit and nature, there is every reason to expect them to behave in the same way. However, CG-MD simulations give very different results for the two models (Fig. 7); their diffusion rates differ by two orders-of-magnitude. The momentum transfer in the Brownian dynamics of the CG-MD simulations is controlled by the damping parameter ω which is related to a mass friction coefficient, $\zeta = m\omega$, where m is the immersed particle mass. The Stokes-Einstein relation

$$D = \frac{k_B T}{\zeta} \,, \tag{12}$$

relates ζ to the diffusion coefficient in linear theory. D is the three-dimensional counterpart of D_{lat}, so ζ does not directly compare to the lateral diffusion, but the proportionality relation between the damping parameter and the diffusion rate in the CG-MD simulations shows that ω can be tuned to produce desirable diffusion rates. The diffusion rates of the BPB and CKD models can only be brought into agreement by using damping parameters that differ with two orders-of-magnitude, without physical motivation, while the integration of the equations of motion is only accurate as long as ω^{-1} is significantly larger than the time step. The particle size, a, plays the role of ω in the SELM simulations, since a determines the magnitude of the neighborhood over which local momentum is dissipated. a is a physical parameter that can not be tuned by orders-of-magnitude like ω, but the diffusion rates from the SELM simulations are still in good agreement with experimental data within the narrow window provided by a.

14

D. Surface shear viscosity

Shear flow was simulated in the direction of the bilayer normal (perpendicular shear), and in the direction of the bilayer plane (parallel shear). The velocity in perpendicular shear only has an x-component that depends on y, $\mathbf{u}(\mathbf{x}) = u_\perp(y)\hat{\mathbf{x}} = sy\hat{\mathbf{x}}$, where s is the shear rate. Perpendicular shear characterizes the bilayer's ability to withstand normal shearing forces, and is measured by the surface shear viscosity, η_s. This is the two-dimensional counterpart to the bulk shear viscosity commonly defined by the Navier-Stokes equations. There is in general no simple relation between the surface shear viscosity of a curved surface and its embedding material, but neglecting surface undulations leads to the thin-film result

$$\eta = \eta_s/h , \tag{13}$$

where h is the film thickness and η is the viscosity of the embedding fluid [45]. η_s is the proportionality coefficient between the shear force (per length) on the bilayer, $F_b/L_\parallel$, and the shear rate s:

$$\eta_s \equiv \frac{F_b/L_\parallel}{s} = \frac{\bar{\sigma}_{xy}L_\perp}{s} . \tag{14}$$

The shear force is equal to the xy-component of the average stress tensor over the xz-plane: $F_b = \bar{\sigma}_{xy}L_\parallel L_\perp$ (molecular simulations often refer to the pressure tensor $\bar{p} = -\bar{\sigma}$), which is determined in a particle simulation from the expression [34]

$$\bar{\sigma}_{\alpha\beta} = -\left\langle \frac{1}{V} \sum_{j \neq i} X_{ij,\alpha} F_{ji,\beta} \right\rangle , \tag{15}$$

with $X_{ji,\alpha}$ being the α-component of the difference vector $\mathbf{X}_{ji} = \mathbf{X}_j - \mathbf{X}_i$ between particle positions j and i, and $F_{ji,\beta}$ being the β-component of the corresponding force. The brackets denote a time average over the simulation trajectory.

Fig. 8 shows Eq. (14) for applied shear rates in the interval 0.001–1.0 /t^0. The trends are similar for both membrane models. η_s depends strongly on s at high rates, but weakens as the shear rate is decreased, and tends to a constant at the lowest rates. The asymptotic value is η_s. A fluid is said to be shear-thinning when the shear viscosity decreases with the shear rate (and shear-thickening when the viscosity increases with the shear rate). Shear-thinning is a common feature of complex fluids, in particular polymeric fluids of elongated molecules. The effect is intuitively understood in the following way: The fluid molecules are aligned at random at low rates, as motions and rotations are prevented by collisions with

15

FIG. 7. (Color online) D_{lat} for the BPB and CKD models, obtained from coarse-grained molecular dynamics (CG-MD) simulations with a Langevin thermostat and no hydrodynamic interactions. ω is the thermostat damping parameter.
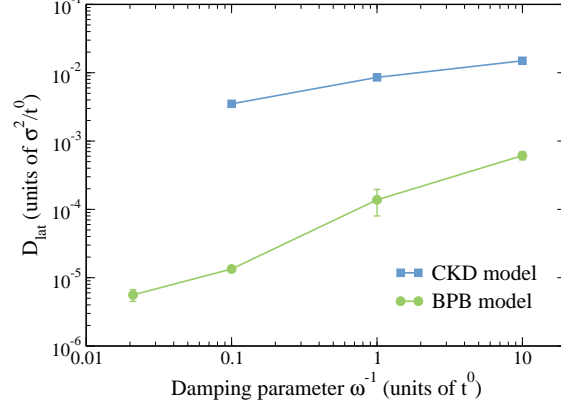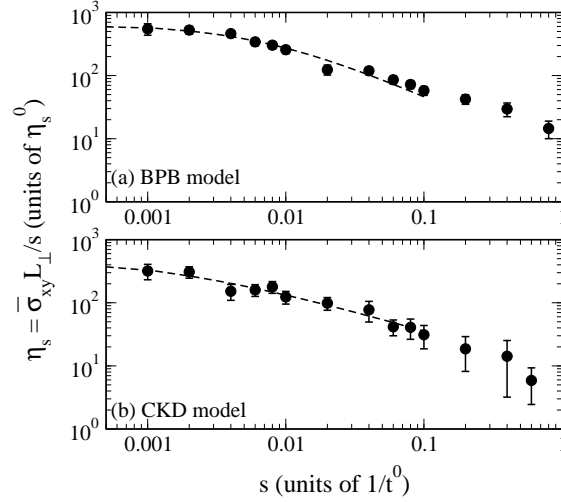

FIG. 8. The surface shear viscosity coefficient, η_s, as a function of shear rate, s for (a) the BPB model and (b) the CKD model. The bilayer is shear-thinning for high rates and levels out as the shear rates approaches zero. The dotted lines are guides to the eye.

other randomly orientated neighbor molecules. The molecules gradually align with the flow direction when the shear rate is increased, and the effective viscosity is lowered. The shear rates in experiments are orders-of-magnitude larger than in simulations. Shearing experiments on lipid systems have essentially reported Newtonian behavior, but shear-thinning has been found at high shear strains [46].

Surface shear viscosities were extracted from the SELM simulations by extrapolation to zero shear rate (Fig. 8). Similar values for η_s were obtained for the two membrane

models, in the range $500\text{--}800\,\eta_s^0$. The higher value corresponds to the BPB model and the lower value to the CKD model. These translate to $\eta_s^{\text{BPB}} = 3.2 \times 10^{-11}$ N s/m and $\eta_s^{\text{CKD}} = 2.2 \times 10^{-11}$ N s/m, respectively, in physical units, numbers that are comparable to previously reported simulation values of higher-detailed membrane models. Shkulipa and co-workers found $\eta_s = 8.5 \times 10^{-13}$ N s/m [47] from shear simulations of a five-bead model with explicit solvent [48]. den Otter and Shkulipa reported $\eta_s = 1.0 \times 10^{-11}$ N s/m [49] from shear simulations of the MARTINI model, which is a 4-to-1-mapping of an atomistic lipid model with explicit solvent [50]. Finally, Müller and Müller-Plathe calculated $\eta_s = 8 \times 10^{-12}$ N s/m [51] (if Eq. (13) is used with $h = 4$ nm to transform their bilayer shear viscosity to a surface shear viscosity) from atomistic simulations. Experimental values are $\sim 10^{-10}$ N s/m [52–54], i.e., one-to-two orders-of-magnitude larger. Measurements that probe macroscopic motions are found to give larger values than techniques that operate on the mesoscopic scale, and the length-scales are in all experimental cases much larger than for the simulations.

Compared to explicit solvent models, the surface shear viscosities calculated from the SELM simulations are somewhat larger than those obtained from highly-detailed membranes (quasi-atomistic MARTINI model and atomistic models). This agreement strongly suggests that the SELM dynamics is as accurate as using the explicit solvent dynamics of a Lennard-Jones fluid. Discrepancies between surface shear viscosities obtained from simulations compared to experiments have been reported earlier [47, 49, 51], and were originally attributed to the simplified coarse-grained membrane models employed in the simulations. However, later simulations of atomistic models have yielded similar values to coarse-grained models. Given the reported range of values for η_s for different models, a more likely explanation is the different length- and time scales probed by simulations and experiments, and/or the interpretations of the experiments. As pointed out by den Otter and Shkulipa [49], liquid-ordered domains near the phase transition temperature could largely impact the bilayer flow properties. Further, membrane undulations have been ignored when analyzing simulation and experimental data. Undulations are negligible in small-patch membrane simulations [55], but can be substantial at the length scales probed by experiments.

E. Inter-monolayer friction

In parallel (to the bilayer normal, with the stagnation plane in the bilayer center) shear, the leaflets slide in opposite directions. The shear velocity is $\mathbf{u}(\mathbf{x}) = u_\|(z)\hat{\mathbf{x}} = sz\hat{\mathbf{x}}$. The friction dissipates energy, which is described by a friction coefficient that plays a similar role to η_s in perpendicular shear. The friction force is such as to oppose lipid motion. The inter-monolayer friction coefficient is hence defined as

$$\xi \equiv \frac{F_f/L_\|^2}{\Delta v}, \tag{16}$$

i.e., as the proportionality constant between the monolayer-monolayer shearing force, F_f, (per area) and the velocity difference between the monolayers, Δv. The friction force acts on the bilayer mid-surface and is equivalent to the xz-component of the average stress tensor over the lateral plane, $F_f = \bar{\sigma}_{xz}L_\|^2$. The friction force results from the monolayers moving as solid material slabs with equal but opposite velocities, Δv. It is difficult to extract the velocity difference with accuracy from the simulations, due to thermal noise. Following Shkulipa et $al.$ [47], Δv was calculated from the distance traveled by the lipid molecules in the flow direction:

$$2\bar{l}^\pm(t) = \pm\Delta v\, t. \tag{17}$$

Here, $\bar{l}^\pm(t) = \bar{x}^\pm(t) - \bar{x}^\pm(0)$ is the average distance traveled by molecules in the top $(+)$ or bottom $(-)$ monolayer in the flow direction (x), at time t. This average was calculated for each time step by the following procedure: A discrete, normalized probability distribution, $w^\pm(l^\pm)$, was determined (independently for the positive and negative displacements) from a histogram of the lipid displacements. The travel distance was calculated by weighted averaging,

$$\bar{l}^\pm = \sum_i l_i^\pm w^\pm(l_i^\pm), \tag{18}$$

where $l_i^\pm$ is the positive or negative displacement of histogram bin i (100 bins were used in total). The velocity difference was obtained as

$$\Delta v = \frac{l^+ - l^-}{t}. \tag{19}$$

Eq. (17) and Eq. (19) predict that $l_\pm$ is linear in time, or consequently, that Δv is independent of time, which is demonstrated in Fig. 9.

18

FIG. 9. The velocity difference, Δv, is calculated from the displacement of lipid molecules. The displacement is linear in time and Δv is determined from the asymptotic value.
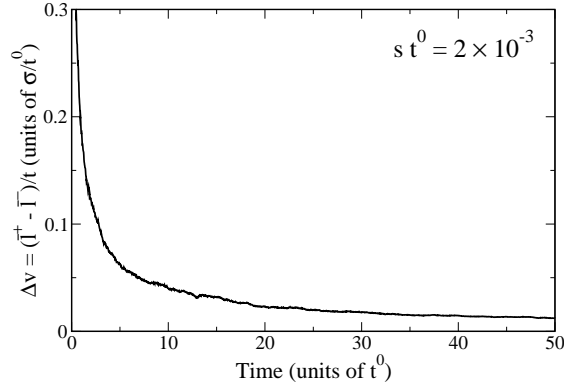

FIG. 10. (a) The inter-monolayer friction coefficient, ξ, as a function of the velocity difference, Δv. In the BPB model (top), the friction is independent of Δv except for the highest velocity differences. In the CKD model (bottom) the dependence is also weak, but there is a slight decrease in friction for the lowest Δv.
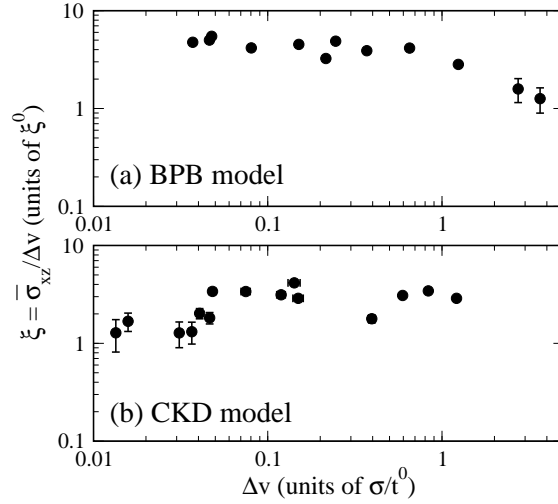

Fig. 10 shows ξ as function of Δv for shear rates in the interval 0.001–$1.0 \, /t^0$. The errors in Δv are largest for the lowest shear rates, because of the small absolute displacements. Despite that Eq. (16) predicts a constant friction coefficient, both membrane models show a weak dependence of ξ on Δv. In the BPB model, the friction coefficient is constant below $\Delta v \sim \sigma/t^0$, while in the CKD model there is a factor-of-two decrease in ξ at the lowest shear rates/velocity differences. Whether the decrease is of physical origin is not clear, since the shearing rates are so low that very long trajectories are required to avoid sampling issues. Friction coefficients were extracted by extrapolation to zero velocity difference, yielding

19

$\xi^{\mathrm{BPB}} = 5\,\xi^0$ and $\xi^{\mathrm{CKD}} = 1.5\,\xi^0$, which translates to $\xi^{\mathrm{BPB}} = 3.7 \times 10^5$ N s/m^3 and $\xi^{\mathrm{CKD}} = 8 \times 10^4$ N s/m^3 in physical units. These values are in line with (albeit slightly smaller than) friction coefficients calculated from atomistic membrane models, using equilibrium [44] and non-equilibrium [51] simulations. Coarse-grained membrane models with explicit solvent [47, 49] have yielded values $\sim 10^6$ N s/m^3.

Experimental values for ξ are more scarce in the literature than those for η_s. Merkel *et al.* [52] used micro-fluorescence techniques to determine monolayer friction coefficients in the interval $(1\text{--}10) \times 10^7$ N s/m^3. Recent experiments on supported lipid bilayers in shear flow [54] used a hydrodynamic model to extract $\xi = 2 \times 10^7$ N s/m^3. These values are consistently about two orders of magnitude larger than the ξ determined from thermal motions in membrane simulations. As for the surface shear viscosity, the explanation for this difference is most likely the different length- and time scales probed by simulations and experiments. The smaller η_s and ξ obtained from the CKD model as compared to the BPB model can be attributed to the short lipid shape. The lipid exchange rate between the leaflets is large in the CKD model [56] and acts to lower the monolayer friction.

A similar thin-film calculation to Eq. (13) yields the approximate relation

$$\xi = \eta/h \,, \tag{20}$$

between the friction coefficient ξ, the bilayer's bulk shear viscosity η, and the film thickness, h. Eliminating the bulk viscosity between Eq. (13) and Eq. (20), gives the crude proportionality relation

$$\alpha \equiv \eta_s/\xi = h^2 \,, \tag{21}$$

between the surface shear viscosity and the monolayer friction coefficient. With experimental values this ratio is somewhat uncertain but ~ 20 nm^2, which corresponds well to the square of the membrane thickness. Defining the thickness in the BPB model as the average distance between the interface beads, and the thickness in the CKD model as the average distance between the head beads, yields $\left(h^{\mathrm{BPB}}\right)^2 = 43.6\,\sigma^2$ and $\left(h^{\mathrm{CKD}}\right)^2 = 22.1\,\sigma^2$. The calculated values for η_s and ξ result in ratios that are about an order-of-magnitude larger than predicted from Eq. (21), $\alpha^{\mathrm{BPB}} = 150\,\sigma^2$ and $\alpha^{\mathrm{CKD}} = 340\,\sigma^2$ for the BPB and CKD models, respectively. Given that the surface viscosities are in rather good agreement with the experimental values, the origin of the discrepancy is the low friction of the membrane models.

V. CONCLUDING REMARKS

The present work has applied Stochastic Eulerian-Lagrangian Methods (SELM) to coarse-grained lipid membrane models. Steady-state and sheared lipid membranes were simulated as fluid-structure systems with overdamped dynamics. SELM simulations show that two coarse-grained membrane models self-assemble, and in contrast to Brownian dynamics simulations, yield dynamic properties in agreement with atomistic simulations. Surface shear viscosities and inter-monolayer friction coefficients were calculated from sheared membranes in agreement to previous highly-detailed simulations with explicit solvent. The membrane models were shown to be shear-thinning over a wide variety of shear rates.

SELM is an immersed boundary method designed to simulate soft matter, that combines the simplicity of particle-based models for microstructures with the equations of fluctuating hydrodynamics. Therefore SELM is highly suitable for condensed-phase simulations of biomolecules in solution, where the solvent particles account for more than 90% of the total particle number. SELM has a computational complexity that is linear, $O(N)$, in the number of immersed particles N [23]; the corresponding scaling is $O(N^3)$ for conventional Stokesian-Brownian dynamics [18], and $O(N^{3/2})$ or slightly lower in more recent implementations [57]. The SELM framework can be used to find systematic and controllable approximations for the hydrodynamic interactions, that give optimal trade-off between efficiency and accuracy.

Membrane dynamics in particular is a rich subject where several relaxation modes of different origins need to be accounted for [58]. Such modes can be probed in spin-echo experiments [59] but the relevant time- and length scales are too large for atomistic simulations. Coarse-grained models are ideal to reach the relevant regimes, but simulation results are not comparable to experimental data or to theoretical predictions [60] if hydrodynamic interactions are neglected. SELM simulation data, however, could remedy this situation and be directly compared to results from elastic theories and experiments.

The present framework can also be applied to lipid vesicles in shear flow, where thermal fluctuations are expected to play a major role [61]. Such vesicles are of high importance in biology, given their similarity in shape and size to red blood cells. Optimization of the numerical algorithm will allow the use of lower shear rates similar to experimental settings, and the overdamped SELM dynamics employed here can be generalized to include inertia and other more subtle hydrodynamic effects.

ACKNOWLEDGMENTS

[1] B. Alberts, A. Johnson, J. Lewis, M. Raff, K. Roberts, and P. Walter, *Molecular Biology of the Cell*, 5th ed. (Garland Science, New York, NY, 2008).

[2] D. Chandler, Nature **437**, 640 (2005).

[3] J. Happel and H. Brenner, *Low Reynolds Number Hydrodynamics with Special Applications to Particulate Media* (Martinus Nijhoff, The Hague, The Netherlands, 1983); M. Doi and S. F. Edwards, *The Theory of Polymer Dynamics* (Oxford University Press, New York, NY, 1986); T. Witten and P. Pincus, *Structured Fluids: Polymers, Colloids, Surfactants* (Oxford University Press, Oxford, UK, 2004).

[4] W. M. Gelbart, A. Ben-Shaul, and D. Roux, eds., *Micelles, Membranes, Microemulsions, and Monolayers* (Springer, New York, NY, 1994).

[5] M. C. Watson, E. S. Penev, P. M. Welch, and F. L. H. Brown, J. Chem. Phys. **135**, 244701 (2011).

[6] U. Seifert and S. A. Langer, Europhys. Lett. **23**, 71 (1993); Biophys. Chem. **49**, 13 (1994).

[7] A. Naji, P. J. Atzberger, and F. L. H. Brown, Phys. Rev. Lett. **102**, 138102 (2009).

[8] B. A. Camley and F. L. H. Brown, Phys. Rev. Lett. **105**, 148102 (2010).

[9] J. M. Ortiz and J. V. Sengers, *Hydrodynamic Fluctuations in Fluids and Mixtures* (Elsevier, Oxford, UK, 2006).

[10] L. Landau and E. M. Lifshitz, *Fluid Mechanics*, 1st ed., Course of Theoretical Physics, Vol. 6 (Addison-Wesley, Reading, MA, 1959).

[11] P. Español, Physica A **248**, 77 (1998).

[12] E. G. Brandt and O. Edholm, Biophys. J. **96**, 1828 (2009).

[13] E. G. Brandt and O. Edholm, J. Chem. Phys. **133**, 115101 (2010).

[14] O. Farago, J. Chem. Phys. **119**, 596 (2003).

[15] G. Brannigan, P. F. Philips, and F. L. H. Brown, Phys. Rev. E **72**, 011915 (2005).

[16] I. R. Cooke, K. Kremer, and M. Deserno, Phys. Rev. E **72**, 011506 (2005).

[17] J. M. Deutch and I. Oppenheim, J. Chem. Phys. **54**, 3547 (1971).

[18] D. L. Ermak and J. A. McCammon, J. Chem. Phys. **69**, 1352 (1978).

[19] J. F. Brady and G. Bossis, Annu. Rev. Fluid Mech. **20**, 111 (1988).

[20] C. S. Peskin, J. Comput. Phys. **25**, 220 (1977).

[21] C. S. Peskin, Acta Numer. **11**, 479 (2002).

[22] P. J. Atzberger, J. Comput. Phys. **230**, 2821 (2011).

[23] P. J. Atzberger, P. R. Kramer, and C. S. Peskin, J. Comput. Phys. **224**, 1255 (2007).

[24] Y. Wang, J. K. Sigurdsson, E. G. Brandt, and P. J. Atzberger, "Dynamic implicit-solvent coarse-grained models of lipid bilayer membranes: Fluctuating hydrodynamics thermostat," (2012), submitted.

[25] P. J. Atzberger, "Stochastic Eulerian-Lagrangian methods for fluid-structure interactions with thermal fluctuations and shear boundary conditions," (2009), arXiv:0910.5739 [cond-mat.soft]; "Incorporating shear into stochastic eulerian lagrangian methods for rheological studies of complex fluids and soft materials," (2012), preprint.

[26] P. J. Atzberger, Phys. D **226**, 144 (2007).

[27] See Supplemental Material at [URL will be inserted by publisher] for additional details on the lipid models and the implementation of the numerical algorithm.

[28] J. K. G. Dhont, *An Introduction to Dynamics of Colloids*, 1st ed., Studies in Interface Science, Vol. 2 (Elsevier, Amsterdam, The Netherlands, 1996).

[29] J. Rotne and S. Prager, J. Chem. Phys. **50**, 4831 (1969); H. Yamakawa, **53**, 436 (1970).

[30] B. Rinn, K. Zahn, P. Maass, and G. Maret, Europhys. Lett. **46**, 537 (1999).

[31] J. F. Brady, R. J. Phillips, J. C. Lester, and G. Bossis, J. Fluid Mech. **195**, 257 (1988).

[32] W. Zylka, J. Chem. Phys. **94**, 4628 (1991).

[33] A. W. Lees and S. F. Edwards, J. Phys. C **5**, 1921 (1972).

[34] M. P. Allen and D. J. Tildesley, *Computer Simulation of Liquids* (Oxford University Press, New York, NY, 1989).

[35] D. J. Evans and O. P. Morriss, Comput. Phys. Rep. **1**, 297 (1984).

[36] R. S. Rogallo, *Numerical Experiments in Homogeneous Turbulence*, NASA Technical Memo-

randum (NASA Ames Research Center, 1981).

[37] H. Kobayashi and R. Yamamoto, J. Chem. Phys. **134**, 064110 (2011).

[38] M. E. Tuckerman, *Statistical Mechanics: Theory and Molecular Simulation*, Oxford Graduate Texts (Oxford University Press, New York, NY, 2010).

[39] P. E. Kloeden and E. Platen, *Numerical Solution of Stochastic Differential Equations*, Stochastic modelling and applied probability No. 23 (Springer, Berlin, Germany, 1992).

[40] S. Plimpton, J. Comput. Phys. **117**, 1 (1995).

[41] T. Schneider and E. Stoll, Phys. Rev. B **17**, 1302 (1978).

[42] L. E. Reichl, *A Modern Course in Statistical Physics*, 2nd ed. (John Wiley & Sons, Inc., New York, NY, 1998).

[43] W. Rawicz, K. C. Olbrich, T. McIntosh, D. Needham, and E. Evans, Biophys. J. **79**, 328 (2000).

[44] J. Wohlert and O. Edholm, J. Chem. Phys. **125**, 204703 (2006).

[45] H. A. Stone, J. Fluid Mech. **645**, 1 (2010).

[46] G. Espinosa, I. López-Montero, F. Monroy, and D. Langevin, Proc. Natl. Acad. Sci. **108**, 6008 (2011).

[47] S. A. Shkulipa, W. K. den Otter, and W. J. Briels, Biophys. J. **89**, 823 (2005).

[48] R. Goetz and R. Lipowsky, J. Chem. Phys. **108**, 7397 (1998).

[49] W. K. den Otter and S. A. Shkulipa, Biophys. J. **93**, 423 (2007).

[50] S. J. Marrink, H. J. Risselada, S. Yefimov, D. P. Tieleman, and A. H. de Vries, J. Phys. Chem. B **111**, 7812 (2007).

[51] T. J. Müller and F. Müller-Plathe, ChemPhysChem **10**, 2305 (2009).

[52] R. Merkel, E. Sackmann, and E. Evans, J. Phys. France **50**, 1535 (1989).

[53] R. Dimova, B. Pouligny, and C. Dietrich, Biophys. J. **79**, 340 (2000).

[54] P. Jönsson, J. P. Beech, J. O. Tegenfeldt, and F. Höök, Langmuir **25**, 6279 (2009).

[55] A. R. Braun, E. G. Brandt, O. Edholm, J. F. Nagle, and J. N. Sachs, Biophys. J. **100**, 2112 (2011).

[56] I. R. Cooke and M. Deserno, J. Chem. Phys. **123**, 224710 (2005).

[57] A. Sierou and J. F. Brady, J. Fluid Mech. **448**, 115 (2001).

[58] U. Seifert, Adv. Phys. **46**, 13 (1997).

[59] M. C. Rheinstädter, T. Seydel, W. Häußler, and T. Salditt, J. Vac. Sci. Technol. A **24**, 1191

(2006).

[60] M. Hömberg and M. Müller, Europhys. Lett. **97**, 68010 (2012).

[61] D. Abreu and U. Seifert, Phys. Rev. E **86**, 010902 (2012).